Growth of nanoscale $BaTiO_3/SrTiO_3$ superlattices by molecular-beam epitaxy

A. Soukiassian,[a] W. Tian,[b] V. Vaithyanathan,[b] J.H. Haeni,[c] L.Q. Chen, X.X. Xi, and D.G. Schlom
Materials Research Institute, The Pennsylvania State University, University Park, Pennsylvania 16802-5005

D.A. Tenne
Department of Physics, Boise State University, Boise, Idaho 83725

H.P. Sun and X.Q. Pan
Department of Materials Science and Engineering, University of Michigan, Ann Arbor, Michigan 48109

K.J. Choi and C.B. Eom
Department of Materials Science and Engineering, University of Wisconsin, Madison, Wisconsin 53706

Y.L. Li and Q.X. Jia
Materials Science and Technology Division, Los Alamos National Laboratory, Los Alamos, New Mexico 87545

C. Constantin and R.M. Feenstra
Department of Physics, Carnegie Mellon University, Pittsburgh, Pennsylvania 15213

M. Bernhagen, P. Reiche, and R. Uecker
Institute for Crystal Growth, Max-Born-Straße 2, D-12489 Berlin, Germany

(Received 29 January 2008; accepted 12 February 2008)

Commensurate $BaTiO_3/SrTiO_3$ superlattices were grown by reactive molecular-beam epitaxy on four different substrates: TiO_2-terminated (001) $SrTiO_3$, (101) $DyScO_3$, (101) $GdScO_3$, and (101) $SmScO_3$. With the aid of reflection high-energy electron diffraction (RHEED), precise single-monolayer doses of BaO, SrO, and TiO_2 were deposited sequentially to create commensurate $BaTiO_3/SrTiO_3$ superlattices with a variety of periodicities. X-ray diffraction (XRD) measurements exhibit clear superlattice peaks at the expected positions. The rocking curve full width half-maximum of the superlattices was as narrow as 7 arc s (0.002°). High-resolution transmission electron microscopy reveals nearly atomically abrupt interfaces. Temperature-dependent ultraviolet Raman and XRD were used to reveal the paraelectric-to-ferroelectric transition temperature (T_C). Our results demonstrate the importance of finite size and strain effects on the T_C of $BaTiO_3/SrTiO_3$ superlattices. In addition to probing finite size and strain effects, these heterostructures may be relevant for novel phonon devices, including mirrors, filters, and cavities for coherent phonon generation and control.

I. INTRODUCTION

Well-ordered $BaTiO_3/SrTiO_3$ superlattices with $BaTiO_3$ and $SrTiO_3$ layer thicknesses in the nanometer range are of interest to probe fundamental issues in ferroelectricity as well as for potential devices. For example, recent theoretical studies predict that (i) the unstrained $SrTiO_3$ layers in $BaTiO_3/SrTiO_3$ superlattices grown commensurately on cubic (100) $SrTiO_3$ substrates are themselves tetragonal and poled by internal electric fields, (ii) the polarization of such superlattices can be enhanced beyond that achievable in unstrained $BaTiO_3$ because of the biaxial compressive strain state of the $BaTiO_3$ layers within the superlattice, and (iii) that ferroelectricity will persist in such superlattices for $BaTiO_3$ layers as thin as the thickness of a single $BaTiO_3$ unit cell (0.4 nm).[1,2]

[a]Address all correspondence to this author.
e-mail: aqs11@psu.edu
[b]Present address: Seagate Technology, Bloomington, MN 55437.
[c]Present address: USAID, Washington, DC 20523.
DOI: 10.1557/JMR.2008.0181

We have begun to experimentally test these predictions[3] and assess oxide heterostructures for phonon confinement[4] by growing commensurate $BaTiO_3/SrTiO_3$ superlattices with a high degree of structural perfection and abrupt interfaces. The thicknesses of the $BaTiO_3$ and $SrTiO_3$ layers (an n unit-cell thick $BaTiO_3$ layer followed by an m unit-cell thick $SrTiO_3$ layer) making up the $BaTiO_3/SrTiO_3$ superlattice repeat unit as well as the number of times p these layers are repeated to form a $[(BaTiO_3)_n/(SrTiO_3)_m]_p$ superlattice must be such to prevent relaxation by the formation of misfit dislocations. Since the critical thickness of a single $BaTiO_3$ film grown on a (001) $SrTiO_3$ substrate is about 4 nm (10 unit cells) for our growth conditions,[5] commensurate $[(BaTiO_3)_n/(SrTiO_3)_m]_p$ superlattices grown on (001) $SrTiO_3$ are limited to $n < 10$ to preserve the high-strain state, $[(a_{SrTiO_3} - a_{BaTiO_3})/a_{BaTiO_3}] = -2.5\%$ for the $BaTiO_3$ film at a growth temperature of 650 °C,[6] and prevent their relaxation. The allowed thickness of the $BaTiO_3$ layers (n unit cells thick) decreases as the number of superlattice repeats p increases.

High-quality $[(BaTiO_3)_n/(SrTiO_3)_m]_p$ superlattices with abrupt interfaces are also of interest for novel acoustic phonon devices including mirrors, filters, and cavities for coherent acoustic phonon generation and control (phonon "laser").[4] The structure of these devices is determined by the acoustic phonon wavelength, which is typically in the range of a few nanometers, indicating that structural quality and interface abruptness is crucial for device performance.

In this paper we focus on the growth of high quality nanoscale $[(BaTiO_3)_n/(SrTiO_3)_m]_p$ superlattices with atomically abrupt interfaces that are vital for the performance of acoustic phonon devices as well as the study of fundamental properties of ferroelectric superlattices. We describe the shuttered reflection high-energy electron diffraction (RHEED) intensity oscillations used in our reactive molecular-beam epitaxy (MBE) process to control film stoichiometry and the n and m unit-cell layer thicknesses of the $BaTiO_3$ and $SrTiO_3$ layers comprising the $[(BaTiO_3)_n/(SrTiO_3)_m]_p$ superlattices. The structural properties of the superlattices grown are described in detail. The improvement of the structural quality of $[(BaTiO_3)_n/(SrTiO_3)_m]_p$ superlattices grown on (101) $DyScO_3$, (101) $GdScO_3$, and (101) $SmScO_3$ substrates[7,8] is also shown. [Throughout this manuscript we use the standard setting of space group no. 62 (*Pnma*) to describe the crystallography of $DyScO_3$, $GdScO_3$, and $SmScO_3$. Although some authors use this setting, many others use the nonstandard setting *Pbnm* to describe the crystallography of $DyScO_3$, $GdScO_3$, $SmScO_3$, and other isostructural perovskites with the $GdFeO_3$ structure, e.g., $NdGaO_3$, $YAlO_3$, and $SrRuO_3$. In the nonstandard setting *Pbnm* the substrates we have used are (110) $GdScO_3$, (110) $DyScO_3$, and (110) $SmScO_3$]. Using these superlattices we demonstrate the importance of strain and finite size effects on the T_C of $[(BaTiO_3)_n/(SrTiO_3)_m]_p$ superlattices with a variety of superlattice thicknesses, constituent layer thicknesses n and m, and strains.

II. EXPERIMENTAL

Epitaxial $[(BaTiO_3)_n/(SrTiO_3)_m]_p$ superlattices were grown on (001) $SrTiO_3$, (101) $DyScO_3$, (101) $GdScO_3$, and (101) $SmScO_3$ substrates by reactive MBE. The strontium and barium fluxes were produced by sublimating elemental strontium and barium contained in titanium crucibles using low-temperature effusion cells. The titanium flux was supplied by a Ti-Ball titanium sublimation pump (Varian Associates, Vacuum Products Division, Lexington, MA).[9] The $[(BaTiO_3)_n/(SrTiO_3)_m]_p$ superlattices were grown by sequential shuttered deposition of the constituent monolayers,[10–12] in a background pressure of 5×10^{-7} Torr of molecular oxygen and a substrate temperature of ~650 °C, as measured by an optical pyrometer. The shuttering timing sequence used to grow a $[(BaTiO_3)_8/(SrTiO_3)_4]_{40}$ superlattice is shown in Fig. 1. A quartz-crystal microbalance (QCM) located directly in front of the substrate was used to get a rough (±5%) idea of the barium, strontium, and titanium molecular beam fluxes. Based on these QCM values, the shuttering times for the deposition of one monolayer of SrO, BaO, and TiO_2 were calculated. These values were used as the starting point for growth on a calibration sample. To determine the shutter opening times more accurately to deposit precise monolayer doses of SrO, BaO, and TiO_2, RHEED was monitored during epitaxial growth on the calibration sample.

Typical RHEED patterns along the [100] and [110] azimuths before and during the growth of a $[(BaTiO_3)_n/(SrTiO_3)_m]_p$ superlattice on a TiO_2-terminated (001) $SrTiO_3$ substrate[13] are shown in Fig. 2. Here white boxes show the area monitored in the analysis of the time evolution of the 00 and 01 streaks. (001) $SrTiO_3$ can have a wide variety of surface reconstructions, depending on stoichiometry, temperature, and oxygen partial pressure.[10,13–15] The RHEED patterns on the TiO_2-terminated (001) $SrTiO_3$ substrates[13] used in this work

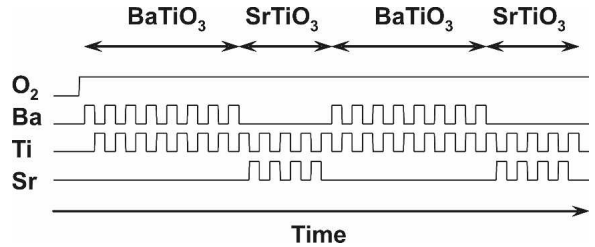

FIG. 1. Timing diagram of the sequential deposition of barium, strontium, and titanium during the growth of two periods of a $(BaTiO_3)_8/(SrTiO_3)_4$ superlattice (sample no. 14). Oxygen is provided continuously during the growth.

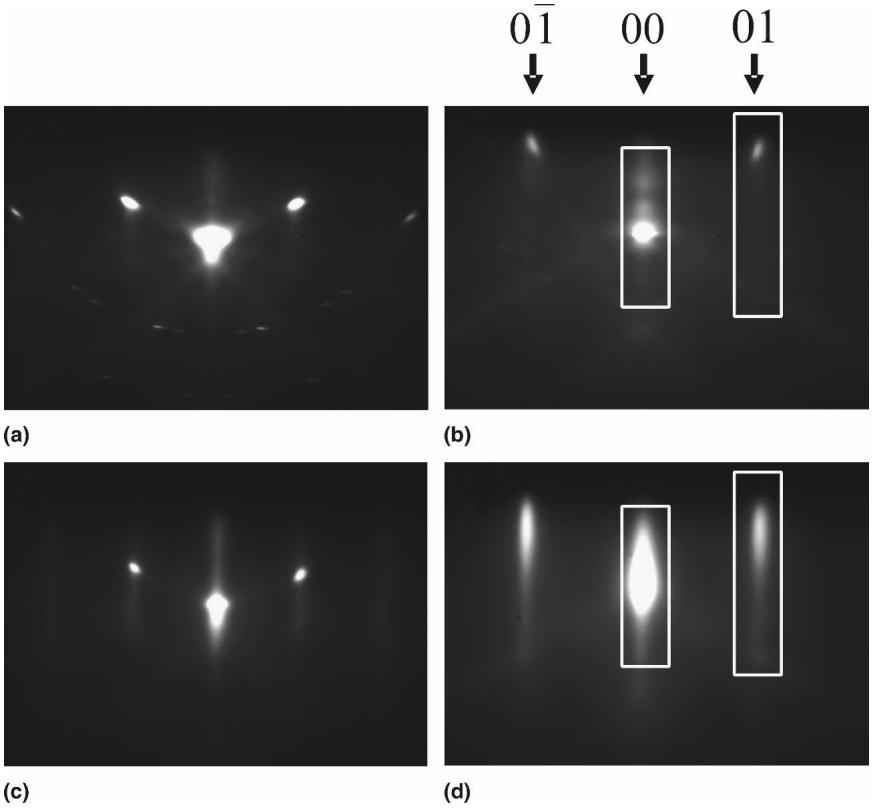

FIG. 2. RHEED patterns during the growth of a $[(BaTiO_3)_8/(SrTiO_3)_4]_{40}$ superlattice (sample no. 14) on a TiO_2-terminated (001) $SrTiO_3$ substrate. RHEED patterns viewed along the [100] azimuth (a) with the substrate at room temperature prior to growth and (c) at T_{sub} = 650 °C during the growth (end of the titanium dose during a $SrTiO_3$ layer). RHEED patterns along the [110] azimuth (b) with the substrate at room temperature prior to the growth and (d) at T_{sub} = 650 °C during the growth (end of the strontium dose during a $SrTiO_3$ layer). The white boxes show the region containing the 00 and 01 streaks that was monitored during growth to establish the time evolution of the RHEED streaks (shuttered RHEED oscillations).

show additional spots (not visible in the zeroth Laue zone). The spots can be seen clearly in the [100] azimuth RHEED pattern [Fig. 2(a)] at room temperature. As the substrate temperature begins to increase, the intensity of the extra spots starts to fade and disappear after about 10 min during heating to the ~650 °C growth temperature in ultrahigh vacuum in the MBE chamber.

By monitoring the changes in the shuttered RHEED intensity oscillations during deposition, film stoichiometry control within ~1% can be achieved for $SrTiO_3$.[16] We found this method to also work for $BaTiO_3$. An example of typical shuttered RHEED oscillations during the growth of a $[(BaTiO_3)_n/(SrTiO_3)_m]_p$ superlattice is shown in Fig. 3. The shuttered RHEED oscillations shown in Fig. 3 were recorded simultaneously along the 00 streak (top) and the 01 streak (bottom) during the growth of three periods of a $[(BaTiO_3)_8/(SrTiO_3)_4]_{40}$ superlattice (sample no. 14). Deposition starts when the barium shutter is opened. The RHEED intensity increases until one monolayer of BaO is deposited. The barium shutter was then closed and the titanium shutter opened, causing the RHEED intensity to decrease until one monolayer of TiO_2 was deposited, completing one

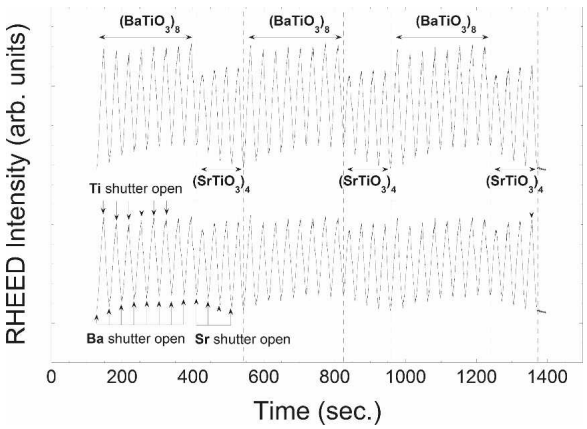

FIG. 3. Shuttered RHEED intensity oscillations observed during the growth of a $[(BaTiO_3)_8/(SrTiO_3)_4]_{40}$ superlattice (sample no. 14). The RHEED beam was incident along the [110] azimuth during growth. Three periods of $[(BaTiO_3)_8/(SrTiO_3)_4]_{40}$ superlattice growth are shown. The average diffracted intensity in the regions shown in Fig. 2(d) of the 00 streak (top) and 01 streak (bottom) were recorded simultaneously. Dashed lines show the boundaries of the $(BaTiO_3)_8$ and $(SrTiO_3)_4$ sections of the superlattice.

unit cell of $BaTiO_3$. Shuttered RHEED oscillations for the growth of unit cells of $SrTiO_3$ are similar to those of $BaTiO_3$. Each peak in Fig. 3 corresponds to the deposition of one unit cell of $BaTiO_3$ or $SrTiO_3$. The deposition rates of SrO, BaO, and TiO_2 were about 15 to 20 s for each monolayer, corresponding to an average growth rate of about 0.1 Å/s.

The total time to deposit the 40 repeats of the $[(BaTiO_3)_8/(SrTiO_3)_4]_{40}$ superlattice (sample no. 14) was more than 5 h. During such a long deposition, fluxes can drift, resulting in changes in film stoichiometry. Therefore, monitoring the shuttered RHEED oscillations during the growth of the $[(BaTiO_3)_n/(SrTiO_3)_m]_p$ superlattices and periodically adjusting the shutter timing was vital to maintaining stoichiometry and accurate monolayer doses during superlattice growth.

An atomically flat substrate surface with a well-defined single termination is required for the reproducible growth of high-quality $[(BaTiO_3)_n/(SrTiO_3)_m]_p$ superlattices with atomically abrupt interfaces. Knowledge of the surface termination is particularly important for our sequential monolayer deposition conditions in which we need to know which species to begin with as we deposit well-calibrated monolayer doses of SrO, BaO, and TiO_2. A well-terminated substrate allows starting with the right material (SrO or BaO in our case) to maintain stoichiometry and grow exact monolayers of $SrTiO_3$ or $BaTiO_3$ from the very beginning, which is important to obtain atomically abrupt interfaces. For this reason we have used the method developed by Koster et al.[13] to prepare TiO_2-terminated (001) $SrTiO_3$ substrates. An atomic force microscopy (AFM) image of a typical TiO_2-terminated $SrTiO_3$ substrate surface prepared by us using this method is shown in Fig. 4(a). The surface has an atomically flat step-terrace structure. Figure 4(b) is a line cut through the data revealing a height of 0.37 ± 0.03 nm, in agreement with the expected 0.3905 nm unit-cell step height of $SrTiO_3$.[17]

The nearly ideal TiO_2 termination of the etched and annealed $SrTiO_3$ substrates can be seen by the RHEED behavior of the shuttered oscillations during the growth of the first several unit cells of the $[(BaTiO_3)_n/(SrTiO_3)_m]_p$ superlattice. If the substrate surface is not fully terminated with TiO_2, the RHEED intensity behavior of the first monolayers of $BaTiO_3$ and $SrTiO_3$ will differ from the steady-state shuttered RHEED intensity oscillations shown in Fig. 3. This difference is seen in Fig. 5 where shuttered RHEED intensity oscillations during the first three periods of a $[(BaTiO_3)_n/(SrTiO_3)_m]_p$ superlattice are recorded from the beginning of growth on a

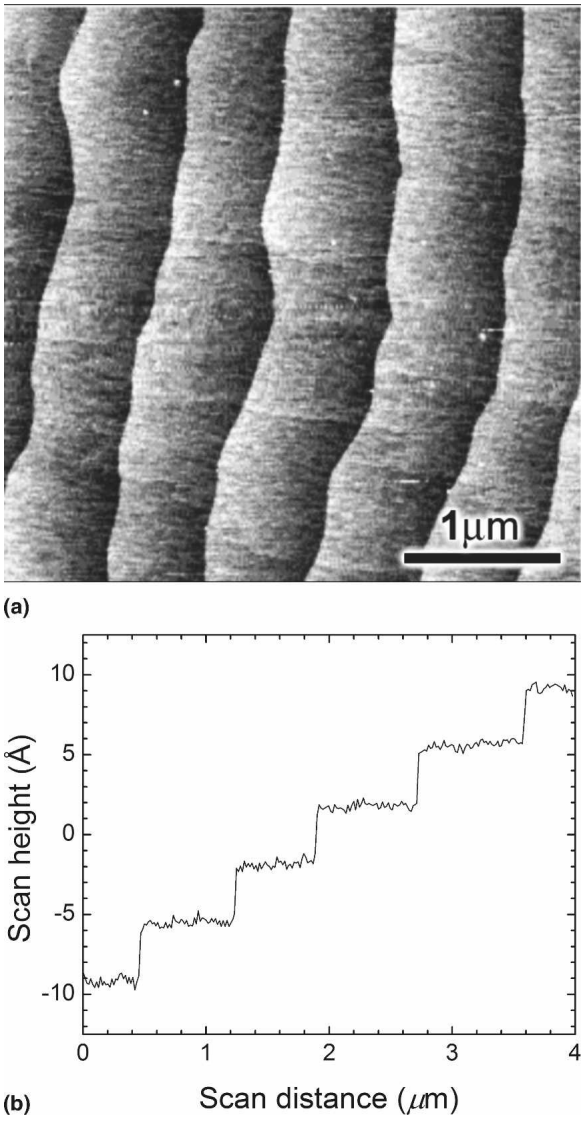

FIG. 4. (a) AFM image of a TiO_2-terminated (001) $SrTiO_3$ substrate prepared using the method described in Ref. 13. The AFM scan extends over 4 μm × 4 μm with a height range of 0.5 nm from black to white. (b) A horizontal line scan across (a) reveals well-defined single-layer steps each ~0.39 nm in height.

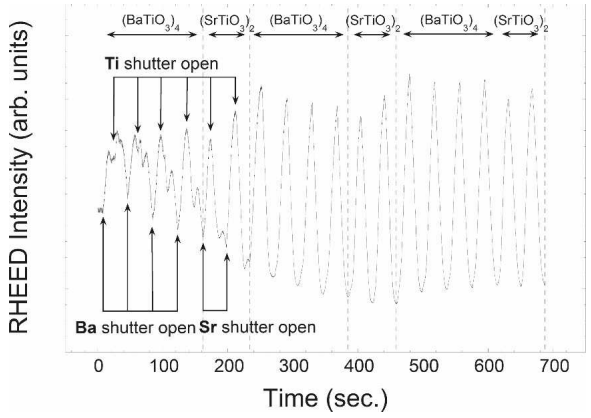

FIG. 5. Shuttered RHEED intensity oscillation observed from the beginning of the growth of a $[(BaTiO_3)_4/(SrTiO_3)_2]_{40}$ superlattice (sample no. 14) on a non-terminated (001) $SrTiO_3$ substrate. The intensity of the 01 RHEED streak along the [110] azimuth for the first three superlattice periods is shown.

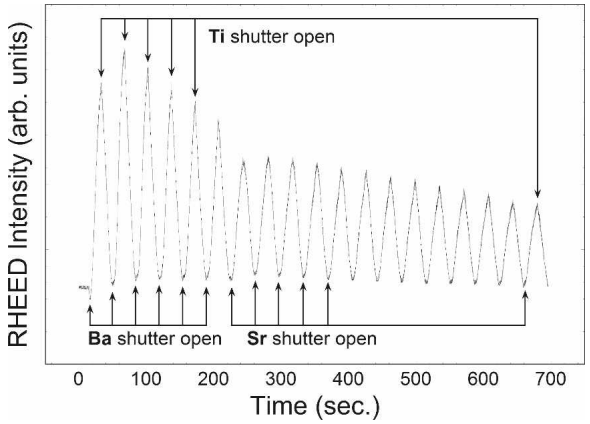

FIG. 6. Shuttered RHEED intensity oscillation observed from the beginning of the growth of a $[(BaTiO_3)_6/(SrTiO_3)_{13}]_{15}$ superlattice (sample no. 12) on a TiO_2-terminated (001) $SrTiO_3$ substrate. The intensity of the 01 RHEED streak along the [110] azimuth of the first superlattice period is shown.

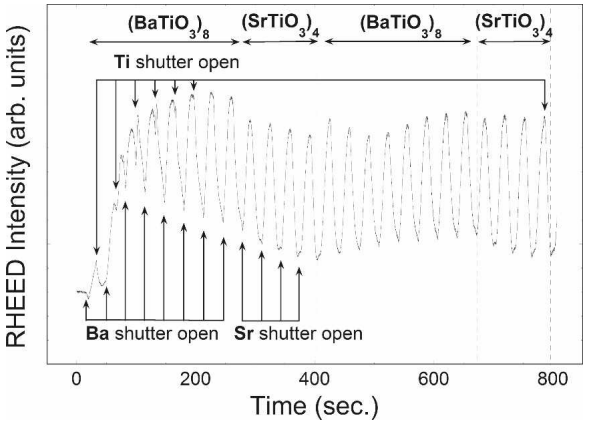

FIG. 7. Shuttered RHEED intensity oscillation observed from the beginning of the growth of a $[(BaTiO_3)_8/(SrTiO_3)_4]_{40}$ superlattice (sample no. 25) on a (101) $GdScO_3$ substrate. The intensity of the 01 RHEED streak along the [110] azimuth for the first two superlattice periods is shown.

nonterminated (001) $SrTiO_3$ substrate in its as-received state from the substrate supplier (CrysTec GmbH, Berlin, Germany). Since the initial (001) $SrTiO_3$ surface is not fully TiO_2 terminated, during the deposition of exactly one monolayer of BaO, only part of the BaO will form $BaTiO_3$ and the excess BaO will make the film surface BaO rich. The subsequent deposition of exactly one monolayer of TiO_2 will again partially form $BaTiO_3$ and leave the surface TiO_2 rich. As a result, the shuttered RHEED intensity oscillation does not vary monotonically during the doses of the constituent monolayers as it does in the case of stoichiometric growth (Fig. 3),

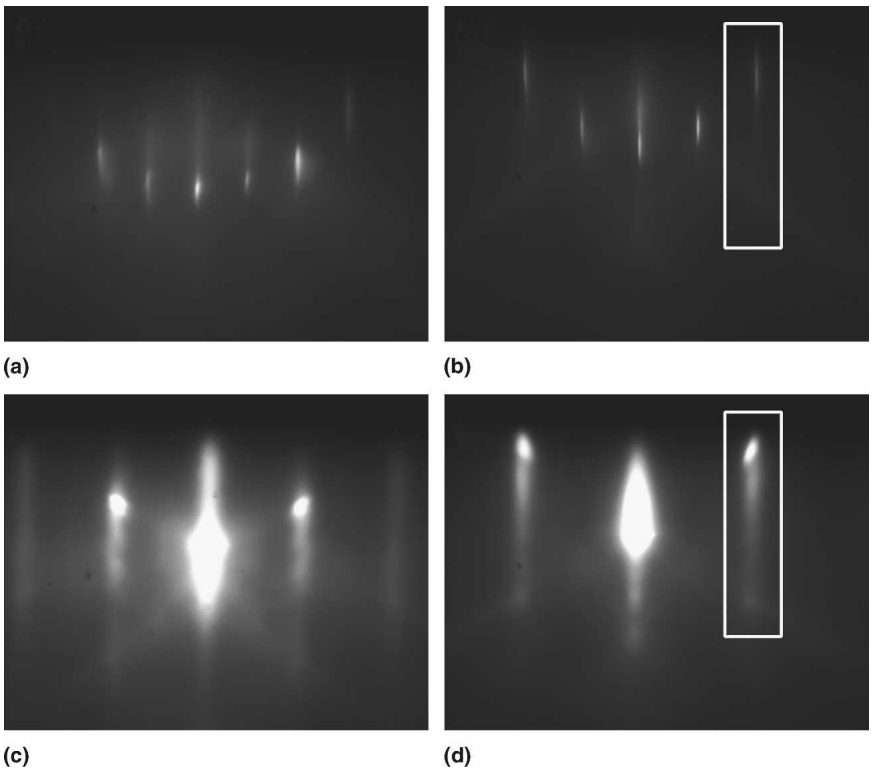

FIG. 8. RHEED patterns during the growth of a $[(BaTiO_3)_8/(SrTiO_3)_4]_{40}$ superlattice (sample no. 25) on a (101) $GdScO_3$ substrate at T_{sub} = 650 °C. RHEED patterns viewed along the [100] pseudocubic azimuth (a) of the bare substrate prior to growth and (c) during the growth (end of the titanium dose during a $SrTiO_3$ layer). RHEED patterns along the [110] pseudocubic azimuth (b) of the bare substrate prior to the growth and (d) during the growth (end of the titanium dose during a $SrTiO_3$ layer). The white boxes show the recorded area of the 01 superlattice streak.

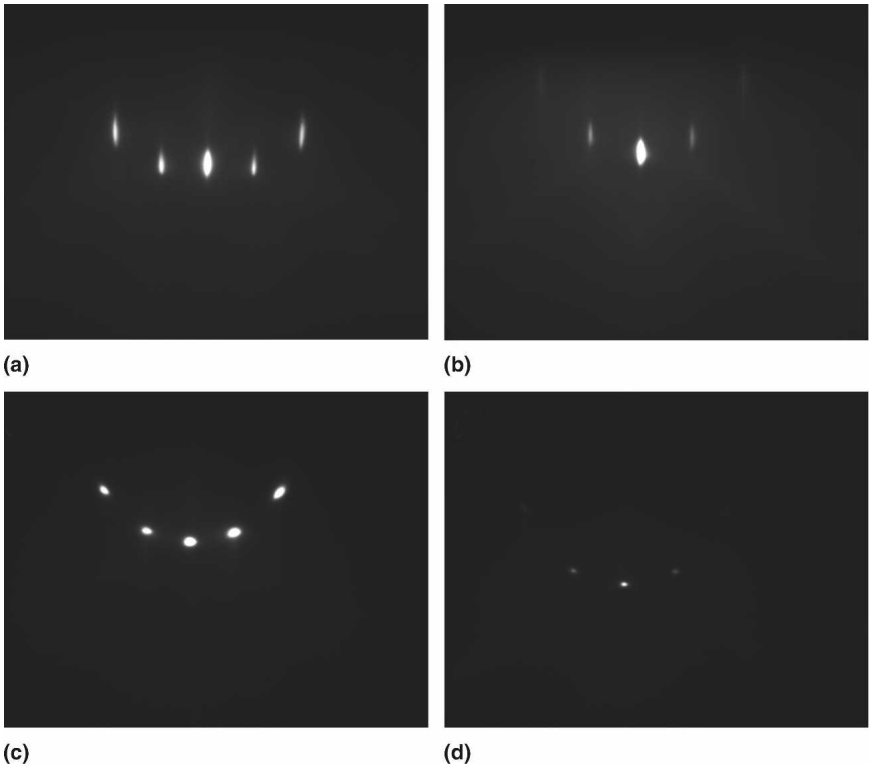

FIG. 9. RHEED patterns of bare (101) $DyScO_3$ substrates at $T_{sub} = 650$ °C prior to growth. RHEED patterns viewed along the [100] pseudocubic azimuth (a) of a nonterminated substrate and (c) a terminated substrate. RHEED patterns along the [110] pseudocubic azimuth (b) of a nonterminated substrate and (d) a terminated substrate.

resulting in the double peaks seen in the initial oscillations in Fig. 5.[16] This RHEED behavior continues until a fully terminated surface is attained at the end of each deposition cycle due to diffusion of the excess BaO, SrO, and TiO_2 into the film. Thus, the deposition of several unit cells of $BaTiO_3$ and $SrTiO_3$ at the beginning of growth takes place before the surface eventually becomes singly terminated in steady state (Fig. 5).

For comparison, shuttered RHEED oscillations from the very beginning of the growth of a $[(BaTiO_3)_6/(SrTiO_3)_{13}]_{15}$ superlattice (sample no. 12) on a TiO_2-terminated $SrTiO_3$ substrate[13] are shown in Fig. 6. The RHEED intensity varies monotonically during each shuttered dose, and no double peaks are observed. This indicates that the growth proceeds via the growth of fully terminated constituent monolayers and is stoichiometric from the very beginning.

The phase shift that a (100) $SrTiO_3$ surface of mixed termination can lead to is likely responsible for the contradictory RHEED intensity behavior for the growth of $SrTiO_3$ layers[18] or $BaTiO_3/SrTiO_3$ superlattices[10,11] reported in the literature. Iijima et al.[10] reported the RHEED intensity to increase during the deposition of barium and strontium and to decrease during the deposition of titanium. Tsurumi et al.[11] reported exactly the opposite behavior. Our observations on substrates of controlled termination are in agreement with the results of Iijima et al.,[10] where the RHEED intensity increases during the deposition of barium and strontium and decreases during titanium.[16]

Shuttered RHEED intensity oscillations during the growth of $[(BaTiO_3)_n/(SrTiO_3)_m]_p$ superlattices on (101) $GdScO_3$, (101) $DyScO_3$, and (101) $SmScO_3$ substrates are similar to those grown on (001) $SrTiO_3$ substrates. Unfortunately, no termination method has been developed for $GdScO_3$ or $SmScO_3$ substrates so far. An alternative method to improve the substrate surface and achieve a single termination could be via the deposition of a homoepitaxial $GdScO_3$ buffer layer that ends at a chosen monolayer prior to the growth of the $[(BaTiO_3)_n/(SrTiO_3)_m]_p$ superlattice. We have not used such an approach, however, in this study. Thus, the shuttered RHEED intensity oscillation behavior for the superlattices grown on (101) $GdScO_3$ are similar to those grown on nonterminated (001) $SrTiO_3$ substrates (Fig. 7). The RHEED patterns along [100] and [110] azimuths of the superlattice before and during the growth of a $[(BaTiO_3)_8/(SrTiO_3)_4]_{40}$ superlattice (sample no. 25) on a (101) $GdScO_3$ substrate are shown in Fig. 8. White boxes show the recorded area of the 01 streak for the shuttered RHEED intensity oscillations shown in Fig. 7.

Blank[19] has developed a method to terminate the surface of (101) $DyScO_3$ substrates. This treatment improves the smoothness of the $DyScO_3$ substrate surface as can be seen

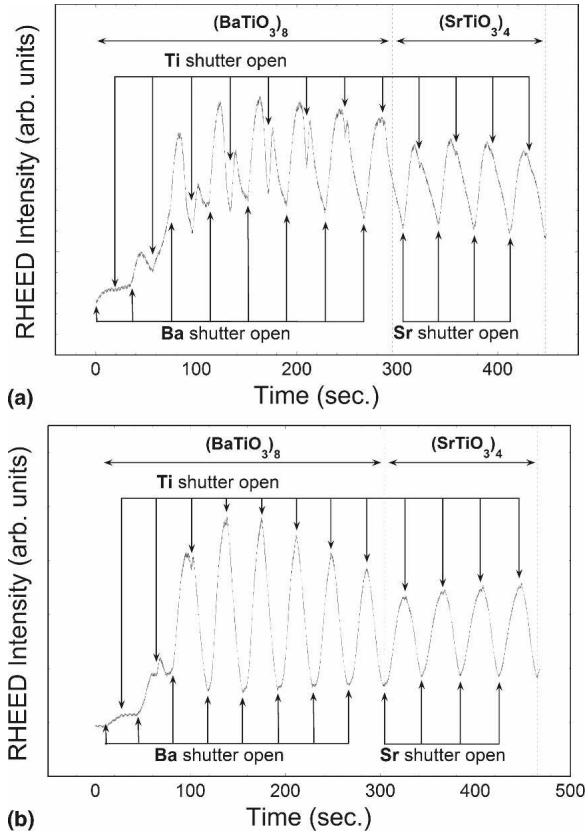

FIG. 10. Shuttered RHEED intensity oscillation observed from the beginning of the growth of a $[(BaTiO_3)_8/(SrTiO_3)_4]_{40}$ superlattice on a nonterminated (a) and terminated (b) (101) $DyScO_3$ substrate. The intensity of the 01 RHEED streak along the [110] azimuth of the first superlattice period is shown.

from comparisons of RHEED patterns of nonterminated and terminated substrates (Fig. 9). A comparison of the shuttered RHEED intensity oscillations during the growth of the first several unit cells of a $[(BaTiO_3)_8/(SrTiO_3)_4]_{40}$ superlattice (sample no. 24) on nonterminated and terminated $DyScO_3$ substrates are shown in Fig. 10. Although the termination method does not provide a fully ScO_2-terminated $DyScO_3$ substrate, it significantly reduces the number of $BaTiO_3$ and $SrTiO_3$ monolayers prior to the onset of steady-state shuttered RHEED intensity oscillations.

Structural characterization of all $[(BaTiO_3)_n/(SrTiO_3)_m]_p$ superlattices was made by four-circle x-ray diffraction (XRD) with Cu K_α radiation using a Picker (Picker Corp., Cleveland, OH) low-resolution XRD and with monochromated Cu $K_{\alpha 1}$ radiation on a Philips X'Pert PRO (PANalytical B.V., Almelo, The Netherlands) high-resolution system. For θ–2θ and ϕ-scans on the Philips X'Pert PRO system a hybrid monochromator was used on the incident beam side, and a 0.27° parallel plate collimator was used on the diffracted beam side. For high-resolution rocking curve measurements, a hybrid monochromator on the incident beam side and a triple-axis arrangement with a 220 Ge analyzer crystal on the diffracted beam side was used. High-resolution transmission electron microscopy (HRTEM) measurements on selected samples were performed in JEOL 3011 and JEOL 2010F (JEOL Ltd., Tokyo, Japan) transmission electron microscopes operated at 400 kV. The T_C of all of the $[(BaTiO_3)_n/(SrTiO_3)_m]_p$ superlattices presented in this paper were obtained from ultraviolet (UV) Raman studies[3] and corroborated by temperature-dependent XRD measurements[20–25] on selected samples.

III. RESULTS AND DISCUSSION

The results of the structural characterization by four-circle XRD of the $[(BaTiO_3)_n/(SrTiO_3)_m]_p$ superlattices are listed in Table I. All samples were grown sequentially with $BaTiO_3$ being the first layer deposited and $SrTiO_3$ the last layer of the superlattice, with the $SrTiO_3$ ending at the TiO_2 monolayer. We grew $[(BaTiO_3)_n/(SrTiO_3)_m]_p$ superlattices with various periodicities including a series with the thickness of the $SrTiO_3$ layer fixed to $m = 4$, 13, and 30 unit cells, while the thickness of the $BaTiO_3$ layer was varied from $n = 1$ to 8 unit cells. θ–2θ x-ray diffraction scans of all of the $[(BaTiO_3)_n/(SrTiO_3)_m]_p$ superlattices were measured and the out-of-plane lattice parameter d of all of the superlattices were obtained from a Nelson–Riley analysis.[26] The measured out-of-plane lattice parameters of the superlattices indicated that all superlattices reported in this work have the targeted number of $BaTiO_3$ and $SrTiO_3$ unit cells in their superlattice units (Table I).

θ–2θ XRD scans of the $[(BaTiO_3)_n/(SrTiO_3)_m]_p$ superlattices with $m = 4$ and $n = 1$, 2, 3, 4, 5, 6, and 8 are shown in Fig. 11. Similarly θ–2θ XRD scans of the $[(BaTiO_3)_n/(SrTiO_3)_m]_p$ superlattices with $m = 13$ and $n = 1$, 2, and 3 are shown in Fig. 12. Nearly all superlattice peaks are present for $2\theta < 55°$, which is an indication of atomically sharp interfaces between the $BaTiO_3$ and $SrTiO_3$ layers. The in-plane orientation relationship between the $[(BaTiO_3)_n/(SrTiO_3)_m]_p$ superlattices and the underlying substrates was determined by an XRD ϕ-scan. A typical ϕ-scan of the 10ℓ peak of a $[(BaTiO_3)_n/(SrTiO_3)_m]_p$ superlattice grown on a (001) $SrTiO_3$ substrate is shown in Fig. 13 (sample no. 14, $[(BaTiO_3)_8/(SrTiO_3)_4]_{40}$). Here $\phi = 0°$ corresponds to when the in-plane component of the diffraction vector is parallel to the [100] in-plane direction of the substrate. It shows that the superlattice is epitaxial with the expected cube-on-cube in-plane alignment with the substrate ([100] of the superlattice is parallel to the [100] of the substrate). The 2θ positions of the 10ℓ superlattice reflections in combination with the measured out-of-plane lattice parameters were used to calculate the in-plane lattice parameters of the superlattices. All $[(BaTiO_3)_n/(SrTiO_3)_m]_p$ superlattices (except sample no. 14, $[(BaTiO_3)_8/(SrTiO_3)_4]_{40}$) grown on

TABLE I. Structural parameters and T_C of $[(BaTiO_3)_n/(SrTiO_3)_m]_p$ superlattices studied in this work.

Sample number	n	m	p	d (Å) (superlattice spacing)	a (Å) (in-plane spacing)	Film FWHM ω (arc s)	Substrate FWHM ω (arc s)	Film thickness (Å)	T_C from UV Raman (K)
1	1	4	50	19.7 ± 0.1	3.905 ± 0.01	45	50	1000	250 ± 20
2	2	4	40	23.8 ± 0.1	3.905 ± 0.01	62	61	950	320 ± 28
3	3	4	35	28.1 ± 0.1	3.905 ± 0.01	21	20	980	350 ± 20
4	4	4	25	32.3 ± 0.5	3.90 ± 0.05	87	79	800	560 ± 21
5	5	4	25	36.3 ± 0.1	3.91 ± 0.01	90	86	900	530 ± 18
6	6	4	20	40.5 ± 0.5	3.91 ± 0.05	320	162	800	510 ± 25
7	8	4	10	48.8 ± 0.2	3.90 ± 0.02	109	96	500	640 ± 17
8	1	13	20	54.9 ± 0.1	3.905 ± 0.01	38	43	1100	170 ± 23
9	2	13	20	59.1 ± 0.1	3.905 ± 0.01	33	35	1200	230 ± 25
10	3	13	20	63.3 ± 0.5	3.905 ± 0.05	55	55	1250	280 ± 19
11	4	13	20	67.6 ± 0.5	3.905 ± 0.05	108	104	1350	380 ± 30
12	6	13	15	75.6 ± 0.5	3.91 ± 0.05	110	118	1130	500 ± 21
13	8	13	15	83.6 ± 0.5	3.90 ± 0.05	55	29	1250	540 ± 24
14	8	4	40	48.3 ± 0.1	3.945 ± 0.01	214	118	1930	440 ± 19
15	1	30	20	121.4 ± 0.5	3.91 ± 0.05	113	139	2430	170 ± 15
16	4	2	40	24.4 ± 0.2	3.90 ± 0.02	33	30	980	520 ± 35
17	4	6	20	40.1 ± 0.1	3.90 ± 0.01	59	57	800	515 ± 27
18	6	1	20	28.5 ± 0.2	3.94 ± 0.02	41	31	570	451 ± 29
19	6	2	20	32.3 ± 0.02	3.945 ± 0.02	143	48	650	421 ± 34
20	6	3	30	36.2 ± 0.2	3.92 ± 0.02	94	59	1100	740 ± 35
21	6	5	20	44.3 ± 0.1	3.91 ± 0.01	26	31	900	615 ± 30
22	6	6	15	48.2 ± 0.1	3.91 ± 0.01	124	71	720	647 ± 28
23	10	5	20	60.4 ± 0.1	3.94 ± 0.01	374	208	1200	440 ± 30
24 ($DyScO_3$)	8	4	40	48.2 ± 0.5	3.95 ± 0.05 (3.945)	9	8	1930	580 ± 17
25 ($GdScO_3$)	8	4	40	48.0 ± 0.5	3.97 ± 0.05 (3.973)	7	7	1930	470 ± 20
26 ($SmScO_3$)	8	4	40	47.75 ± 0.05	3.993 ± 0.005 (3.987)	9	9	1930	398 ± 25

Here n is the $BaTiO_3$ thickness in unit cells, m is the $SrTiO_3$ thickness in unit cells, and p is the number of periods. For the samples grown on (101) $DyScO_3$, (101) $GdScO_3$, and (101) $SmScO_3$ substrates, the measured pseudocubic lattice constant a_p is shown in parentheses.

$SrTiO_3$ substrates are commensurate and have measured in-plane lattice constants that are the same (within the experimental error of our measurements) as that of the $SrTiO_3$ substrate ($a = 3.905$ Å, Table I).

Rocking curves of the $[(BaTiO_3)_n/(SrTiO_3)_m]_p$ superlattices were measured on the strongest superlattice 00ℓ peaks that were well separated from the substrate peaks. Rocking curves of the underlying substrates were measured on the 002 $SrTiO_3$, 202 $GdScO_3$, 202 $DyScO_3$, and 202 $SmScO_3$ peaks. The rocking curve (ω-scans) full widths half-maximum (FWHM) of the superlattices and underlying substrates are shown in Table I. The rocking curve measurements on $SrTiO_3$ substrates reveal that nearly all of them exhibit mosaic features (subgrain boundaries) resulting in a large spread in measured ω FWHM values from as low as 20 arc s (0.0055°) to 208 arc s (0.0578°) for the (001) $SrTiO_3$ substrates used in this work (CrysTec GmbH, Berlin, Germany) (Table I). Moreover, different regions of the $SrTiO_3$ substrate may also have different ω FWHM due to the highly inhomogeneous mosaic spread of commercial $SrTiO_3$ single crystals.[27] For this reason, rocking curve comparisons between the $[(BaTiO_3)_n/(SrTiO_3)_m]_p$ superlattices and the substrates on which they were grown were always measured on the same region of the substrate.

As an example, rocking curves of two $[(BaTiO_3)_n/(SrTiO_3)_m]_p$ superlattices grown on (001) $SrTiO_3$ substrates with a one single narrow peak (sample no. 3, $[(BaTiO_3)_3/(SrTiO_3)_4]_{35}$) and another with a strongly mosaic peak (sample no. 2, $[(BaTiO_3)_2/(SrTiO_3)_4]_{40}$), are shown in Fig. 14. Rocking curves of the $[(BaTiO_3)_3/(SrTiO_3)_4]_{35}$ superlattice 00$\underline{14}$ peak (sample no. 3) and the underlying $SrTiO_3$ substrate 002 peak (at the same position on the substrate) are shown in Fig. 14(a). The ω FWHM is 21 arc s (0.0058°) for the superlattice peak compared with 20 arc s (0.0055°) for the substrate peak. The sharp rocking curve indicates the high structural perfection of the superlattice. For comparison, the rocking curves of the $[(BaTiO_3)_2/(SrTiO_3)_4]_{40}$ superlattice 00$\underline{12}$ peak (sample no. 2) and the underlying $SrTiO_3$ substrate 002 peak are shown in Fig. 14(b). The ω FWHM is 62 arc s (0.0172°) for the superlattice peak as compared with 61 arc s (0.0169°) for the substrate peak with multiple

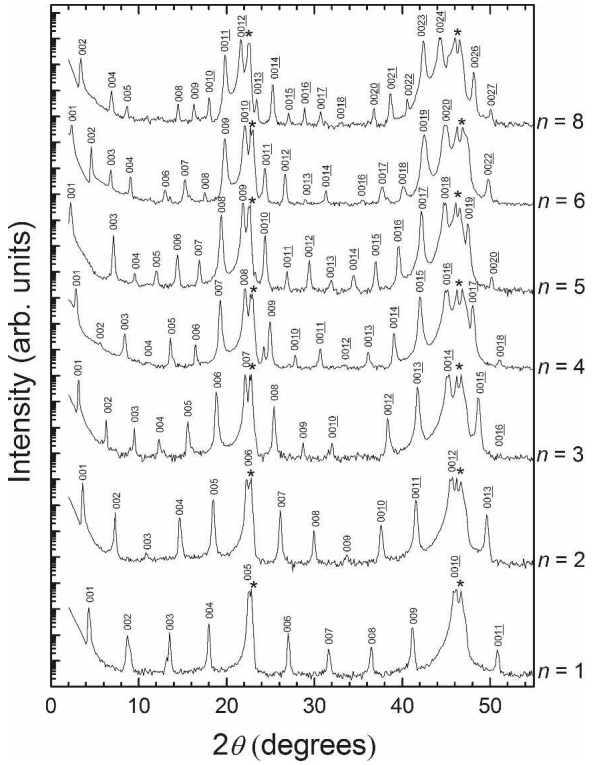

FIG. 11. θ–2θ XRD scans of the $[(BaTiO_3)_n/(SrTiO_3)_m]_p$ superlattices using Cu K_α radiation for $m = 4$ and $n = 1$, 2, 3, 4, 5, 6, and 8 (samples no. 1–7). Substrate peaks are marked with asterisks (*). Nearly all superlattice peaks are present for $2\theta < 55°$, indicating atomically sharp interfaces between the $BaTiO_3$ and $SrTiO_3$ layers and accurate superlattice periodicity.

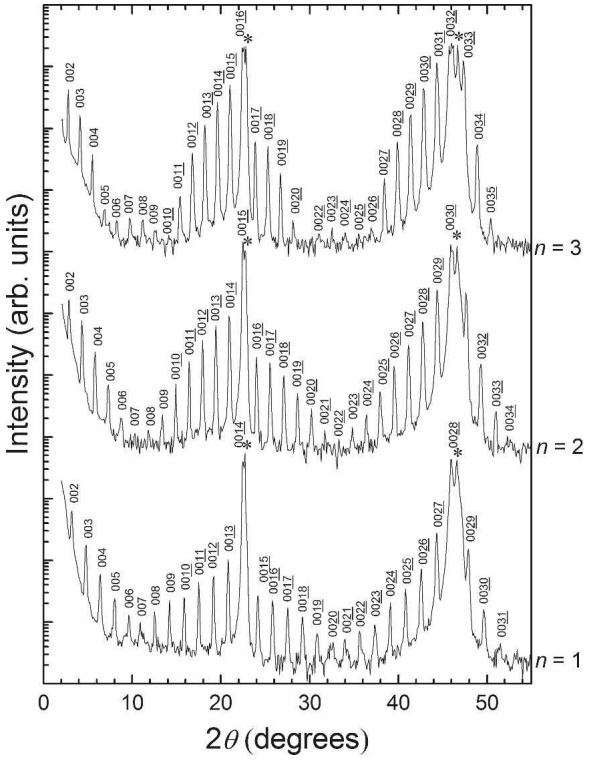

FIG. 12. θ–2θ XRD scans of the $[(BaTiO_3)_n/(SrTiO_3)_m]_p$ superlattices using Cu K_α radiation for $m = 13$ and $n = 1$, 2, and 3 (samples no. 8–10). Substrate peaks are marked with asterisks (*). Nearly all superlattice peaks are present for $2\theta < 55°$, indicating atomically sharp interfaces between the $BaTiO_3$ and $SrTiO_3$ layers and accurate superlattice periodicity.

mosaic features. Both samples in Fig. 14 are commensurate as indicated from the in-plane lattice parameters.

We noticed that the ω FWHM of all commensurate samples had similar ω FWHM values as their underlying substrates, showing that the crystalline quality of the superlattices is limited by that of the underlying substrates. Sample no. 6, the $[(BaTiO_3)_6/(SrTiO_3)_4]_{20}$ superlattice, grown on a $SrTiO_3$ substrate with poor crystallinity [ω FWHM = 162 arc s (0.0451°)] shows a large ω FWHM = 320 arc s (0.0890°). We suspect that the increase in the ω FWHM of this superlattice is caused by an increase in its dislocation density, which can result in the lowering of T_C. Relaxation may occur also if the critical thickness of the superlattice is exceeded. An ~1930 Å thick $[(BaTiO_3)_8/(SrTiO_3)_4]_{40}$ superlattice grown on a (001) $SrTiO_3$ substrate (sample no. 14) is not commensurate and has an in-plane lattice parameter of $a = 3.945 \pm 0.01$ Å. This indicates that the $[(BaTiO_3)_8/(SrTiO_3)_4]_{40}$ superlattice is partially relaxed and is only strained by $\epsilon = -1.05\%$, rather than the $\epsilon = -2.3\%$ biaxial compressive strain that it would be under if it were still commensurate. As a result, the ferroelectric phase transition temperature is significantly decreased ($T_C \approx 440$ K) compared with the commensurate sample no. 7 ($T_C \approx 640$ K), which has a similar $[(BaTiO_3)_8/$

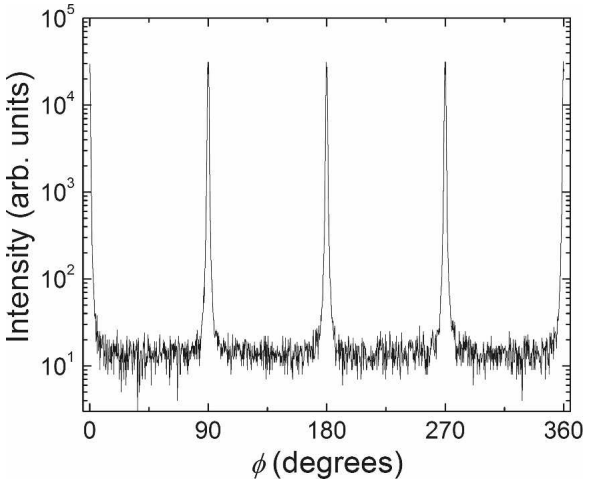

FIG. 13. XRD φ scan at $\chi = 44.3°$ of the $10\underline{12}$ peak of the $[(BaTiO_3)_8/(SrTiO_3)_4]_{40}$ superlattice (sample no. 14) grown on a (001) $SrTiO_3$ substrate. $\chi = 90°$ aligns the diffraction vector to be perpendicular to the plane of the substrate. $\phi = 0°$ corresponds to when the in-plane component of the diffraction vector is parallel to the [100] in-plane direction of the substrate. This scan shows that the superlattice is epitaxial with the expected ([100] superlattice ∥ [100] substrate) in-plane alignment with the substrate.

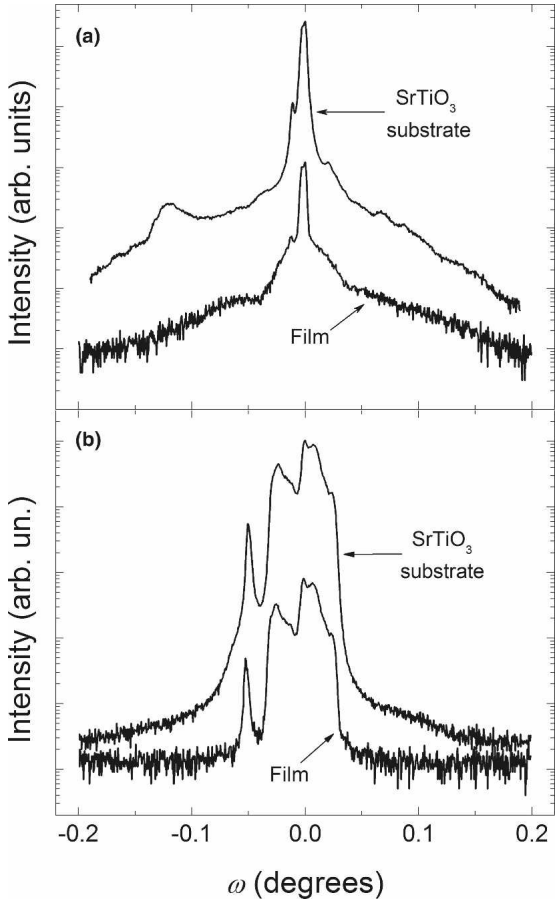

FIG. 14. (a) Rocking curves of the $[(BaTiO_3)_3/(SrTiO_3)_4]_{35}$ superlattice 00$\underline{14}$ peak and the underlying $SrTiO_3$ substrate 002 peak (sample no. 3). The FWHM is 21 arc s (0.0058°) for the superlattice peak as compared to 20 arc s (0.0055°) for the substrate peak. The sharp rocking curve indicates the high structural perfection of the superlattice. (b) Rocking curves of the $[(BaTiO_3)_2/(SrTiO_3)_4]_{40}$ superlattice 00$\underline{12}$ peak and the underlying $SrTiO_3$ substrate 002 peak (sample no. 2). The FWHM is 62 arc s (0.0172°) for the superlattice peak compared with 61 arc s (0.0169°) for the substrate peak having a strongly mosaic feature.

$(SrTiO_3)_4]_{10}$ structure, but is thinner (~500 Å).[3] The critical thickness for relaxation in the $BaTiO_3/SrTiO_3$ superlattices grown on (001) $SrTiO_3$ substrates depends on the layer thicknesses of both $BaTiO_3$ and $SrTiO_3$. For superlattices containing the same total thickness of $BaTiO_3$, those with thicker $SrTiO_3$ layers separating the $BaTiO_3$ layers had higher critical thicknesses. For example, $[(BaTiO_3)_6/(SrTiO_3)_1]_{20}$ and $[(BaTiO_3)_6/(SrTiO_3)_2]_{20}$ superlattices (samples no. 18 and 19) grown on (001) $SrTiO_3$ substrates having $SrTiO_3$ layer thicknesses as thin as one- and two-unit cells, respectively, are partially relaxed indicating that critical thickness in these samples are significantly smaller than in the superlattices having thicker $SrTiO_3$ layers, e.g., $[(BaTiO_3)_6/(SrTiO_3)_5]_{20}$ superlattice (samples no. 21). Relaxation also occurred in the superlattices consisting of 10 and more unit cells of $BaTiO_3$ in the layers. For example, a $[(BaTiO_3)_{10}/(SrTiO_3)_5]_{20}$ superlattice (sample no. 23) has an in-plane lattice parameter of $a = 3.94 \pm 0.01$ Å and is partially relaxed.

The mechanism of superlattice relaxation has been studied by TEM and is found to be the introduction of misfit dislocations, which form dislocation half loops with threading dislocation segments that extend through the entire film. Figure 15(a) is a cross-sectional HRTEM image showing a threading dislocation in this partially relaxed $[(BaTiO_3)_8/(SrTiO_3)_4]_{40}$ superlattice (sample no. 14) that extends through the film. These threading dislocations may also be seen in the *Z*-contrast TEM image from a larger area of the same $[(BaTiO_3)_8/(SrTiO_3)_4]_{40}$ superlattice, Fig. 15(b), where they show up as the lighter regions (see arrows). The $[(BaTiO_3)_8/(SrTiO_3)_4]_{40}$ superlattice (sample no. 14) has a large ω FWHM of 214 arc s (0.0595°) compared with the substrate ω FWHM of 118 arc s (0.0328°), consistent with the superlattice having a high density of misfit dislocations.

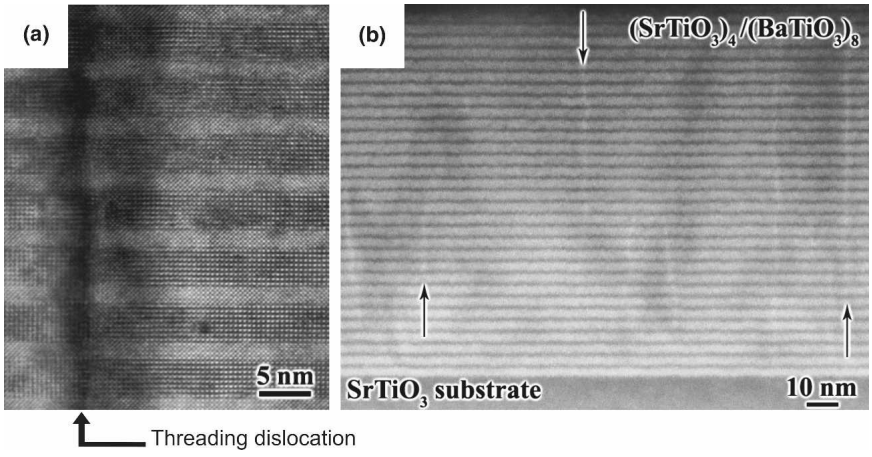

FIG. 15. (a) Cross-sectional HRTEM image of the partially relaxed $[(BaTiO_3)_8/(SrTiO_3)_4]_{40}$ superlattice grown on a (001) $SrTiO_3$ substrate (sample no. 14) showing threading dislocation. (b) Z-contrast TEM over a larger area of the same $[(BaTiO_3)_8/(SrTiO_3)_4]_{40}$ superlattice (sample no. 14). The threading dislocations are the light vertical defects, some of which are labeled with arrows.

Unlike the partially relaxed $[(BaTiO_3)_8/(SrTiO_3)_4]_{40}$ superlattice, no threading dislocations were observed in the commensurate $[(BaTiO_3)_n/(SrTiO_3)_m]_p$ superlattices studied by HRTEM. Figure 16 shows two cross-sectional HRTEM examples from commensurate $[(BaTiO_3)_n/(SrTiO_3)_m]_p$ superlattices (samples no. 1 and 8). The TEMs (both HRTEM and *Z*-contrast TEM) reveal superlattices with nearly atomically abrupt interfaces and no observable dislocations.

The last three rows of Table I contain data from $[(BaTiO_3)_8/(SrTiO_3)_4]_{40}$ superlattices grown on (101) $DyScO_3$ (sample no. 24), (101) $GdScO_3$ (sample no. 25), and (101) $SmScO_3$ (sample no. 26). All samples are commensurate with the underlying substrates despite the fact that the thickness and structure of these samples are the same as the partially relaxed sample no. 14 grown on $SrTiO_3$, i.e., all are $[(BaTiO_3)_8/(SrTiO_3)_4]_{40}$ superlattices. The measured in-plane lattice parameter of sample no. 24 is $a = 3.945 \pm 0.05$ Å compared with the measured pseudocubic lattice parameter of the underlying $DyScO_3$ substrate $a_p = 3.945$ Å (shown in Table I in parentheses). This is due to $BaTiO_3$ undergoing a smaller compressive strain, $\epsilon \approx -1.7\%$, when grown on (101) $DyScO_3$ than on (001) $SrTiO_3$. Thus, the critical thicknesses of individual $BaTiO_3$ layers and of the whole $[(BaTiO_3)_n/(SrTiO_3)_m]_p$ superlattice are much larger.[20] The $SrTiO_3$ layers of this superlattice are under biaxial tension, $\epsilon \approx 1\%$. Similarly, the $[(BaTiO_3)_8/(SrTiO_3)_4]_{40}$ grown on (101) $GdScO_3$ (sample no. 25) is also found to be commensurate. Here the $BaTiO_3$ layers are under an even smaller compressive strain ~1%, while the $SrTiO_3$ layers are under biaxial tensile strain of ~1.7%.[20] The $[(BaTiO_3)_8/(SrTiO_3)_4]_{40}$ grown on (101) $SmScO_3$ (sample no. 26) can be considered to be opposite to the one grown on (001) $SrTiO_3$ since the in-plane lattice parameters of the $SmScO_3$ substrate and $BaTiO_3$ are nearly same (i.e., almost no strain is applied to the $BaTiO_3$ layers by the underlying substrate, while the $SrTiO_3$ layers are under a large biaxial tensile strain of ~2.2%). In superlattices grown commensurately on $SrTiO_3$ substrates, the unstrained $SrTiO_3$ layers are polar because of the presence of neighboring ferroelectric $BaTiO_3$ layers,[3] while in superlattices grown on $DyScO_3$, $GdScO_3$, and $SmScO_3$ substrates the $SrTiO_3$ layers are strained and exhibit strain-induced ferroelectricity[28–30] in addition to the polarization induced by the $BaTiO_3$.

Structural characterization of $[(BaTiO_3)_8/(SrTiO_3)_4]_{40}$ superlattices grown on (101) $DyScO_3$, (101) $GdScO_3$, and (101) $SmScO_3$ substrates reveals a significant improvement in the superlattice crystalline perfection compared with the superlattices grown on (001) $SrTiO_3$ substrates. The XRD scans of a $[(BaTiO_3)_8/(SrTiO_3)_4]_{40}$ superlattice grown on a (101) $DyScO_3$ substrate (sample no. 24) are shown in Fig. 17. Nearly all superlattice peaks show up in the θ–2θ XRD scan [Fig. 17(a)]. The

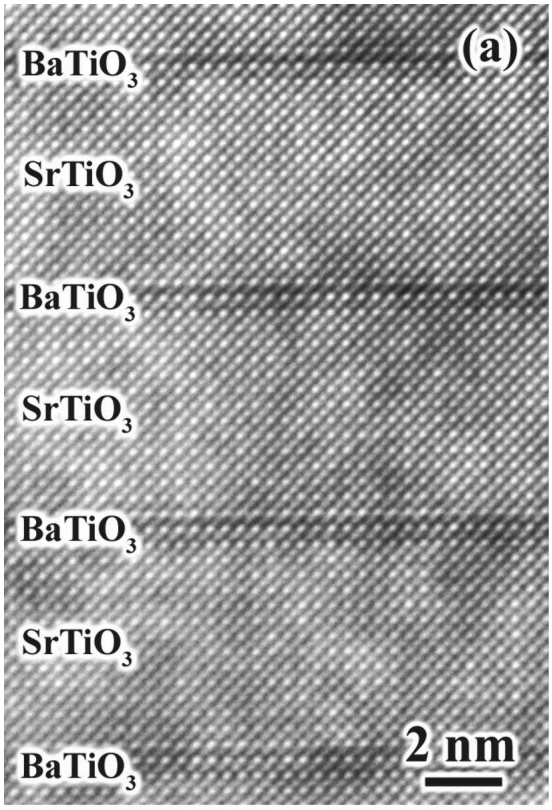

(a)

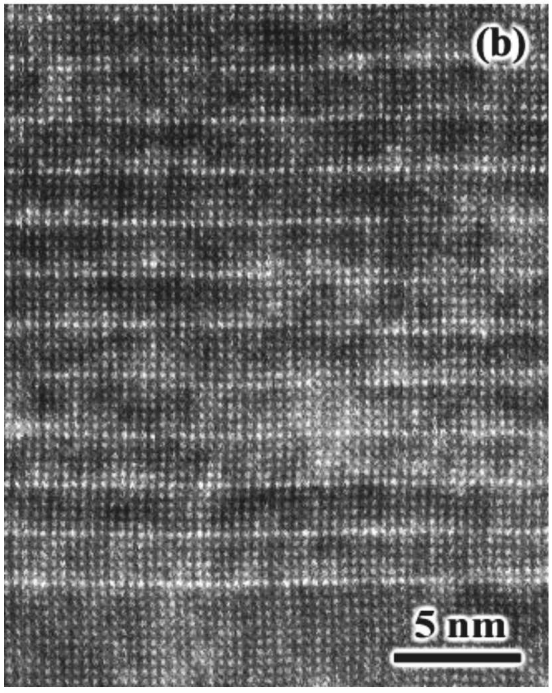

(b)

FIG. 16. (a) Cross-sectional HRTEM image of the $[(BaTiO_3)_1/(SrTiO_3)_{13}]_{20}$ superlattice (sample no. 8). It shows alternating layers of 1 unit cell of $BaTiO_3$ and 13 unit cells of $SrTiO_3$, confirming the intended superlattice periodicity and the XRD result. (b) Z-contrast HRTEM image of the $[(BaTiO_3)_1/(SrTiO_3)_4]_{50}$ superlattice (sample no. 1). The interfaces are abrupt, and no misfit dislocations were seen.

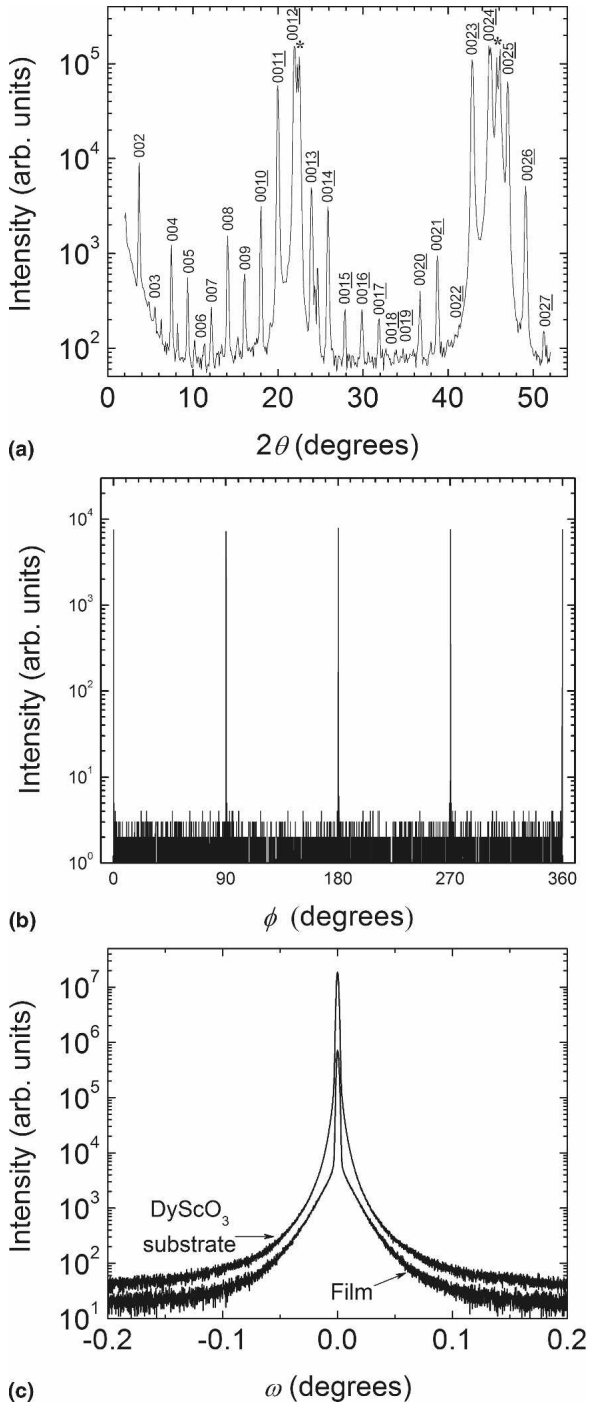

FIG. 17. XRD scans of the $[(BaTiO_3)_8/(SrTiO_3)_4]_{40}$ superlattice grown on (101) $DyScO_3$ substrate (sample no. 24) (a) shows a θ–2θ scan. Substrate peaks are marked with asterisks (*). Nearly all superlattice peaks are present for $2\theta < 55°$, indicating atomically sharp interfaces between $BaTiO_3$ and $SrTiO_3$ layers and accurate periodicity. (b) The in-plane orientation relationship between the $[(BaTiO_3)_8/(SrTiO_3)_4]_{40}$ superlattice and the (101) $DyScO_3$ substrate was determined by a φ-scan at $\chi = 45°$ of the $10\underline{1}2$ superlattice peak. $\phi = 0°$ corresponds to when the in-plane component of the diffraction vector is parallel is aligned parallel to the [010] in-plane direction of the $DyScO_3$ substrate. (c) Rocking curves of the same $[(BaTiO_3)_8/(SrTiO_3)_4]_{40}$ superlattice and the underlying $DyScO_3$ substrate FWHM of 9 arc s (0.0024°) for the superlattice $00\underline{2}4$ peak and FWHM of 8 arc s (0.0022°) for the 202 peak of the $DyScO_3$ substrate were measured.

in-plane orientation relationship between the $[(BaTiO_3)_8/(SrTiO_3)_4]_{40}$ superlattice and the (101) $DyScO_3$ substrate was determined by a φ-scan of the $10\underline{1}2$ superlattice peak [Fig. 17(b)]. In this scan, $\phi = 0°$ corresponds to when the in-plane component of the diffraction vector is aligned parallel to the [010] in-plain direction of the $DyScO_3$ substrate. It shows that the superlattice is epitaxial with the expected ([100] superlattice ‖ [010] substrate) in-plane alignment with the substrate. Rocking curves of the $[(BaTiO_3)_8/(SrTiO_3)_4]_{40}$ superlattice and the underlying $DyScO_3$ substrate are shown on Fig. 17(c). The FWHM in ω of the superlattice $00\underline{2}4$ peak and of the 202 peak of the underlying $DyScO_3$ substrate were found to be 9 arc s (0.0024°) and 8 arc s (0.0022°), respectively.

Similar XRD scans of a $[(BaTiO_3)_8/(SrTiO_3)_4]_{40}$ superlattice grown on a (101) $GdScO_3$ substrate (sample no. 25) are shown in Fig. 18. Again nearly all superlattice peaks are seen in the θ–2θ XRD scan [Fig. 18(a)]. Since the compressive mismatch strain imposed by the $GdScO_3$ substrate on $BaTiO_3$ is smaller, and the tensile strain imposed on $SrTiO_3$ is larger than in sample no. 24, the out-of-plane lattice parameter $d = 48.0 \pm 0.5$ Å is smaller than $d = 48.2 \pm 0.5$ Å for sample no. 24 and even smaller than $d = 48.8 \pm 0.2$ Å in sample no. 7 with the largest mismatch strain. The in-plane orientation relationship between the $[(BaTiO_3)_8/(SrTiO_3)_4]_{40}$ superlattice (sample no. 25) and the (101) $GdScO_3$ substrate was determined by a φ-scan of the $10\underline{1}1$ superlattice peak [Fig. 18(b)]. This φ-scan shows that the superlattice is epitaxial with the same in-plane alignment with the substrate as the superlattice grown on $DyScO_3$ ([100] superlattice ‖ [010] substrate). Rocking curves of the $[(BaTiO_3)_8/(SrTiO_3)_4]_{40}$ superlattice and the underlying $GdScO_3$ substrate are shown in Fig. 18(c). The rocking curve FWHM in ω of the superlattice $00\underline{2}4$ peak was 7 arc s (0.0020°), and that of the 202 peak of the underlying $GdScO_3$ substrate was 7 arc s (0.0019°).

Our results indicate that the structural perfection of the $[(BaTiO_3)_n/(SrTiO_3)_m]_p$ superlattices depend on the structural perfection of the substrate they are grown on. When the underlying substrates have very high structural perfection, i.e., $DyScO_3$, $GdScO_3$, and $SmScO_3$, the commensurate $[(BaTiO_3)_8/(SrTiO_3)_4]_{40}$ superlattices have very high structural perfection. This indicates that $[(BaTiO_3)_n/(SrTiO_3)_m]_p$ superlattices, if grown on high-quality $DyScO_3$, $GdScO_3$, and $SmScO_3$ substrates, can have better structural perfection than any commercially available $SrTiO_3$ substrate[31–33] or films grown on such substrates. The rocking curves of our $[(BaTiO_3)_8/(SrTiO_3)_4]_{40}$ superlattices grown on $DyScO_3$, $GdScO_3$, and $SmScO_3$ substrates are by far the narrowest ever reported for oxide superlattices.

An important advantage of using $DyScO_3$, $GdScO_3$, and $SmScO_3$ substrates is that these rare-earth scandate

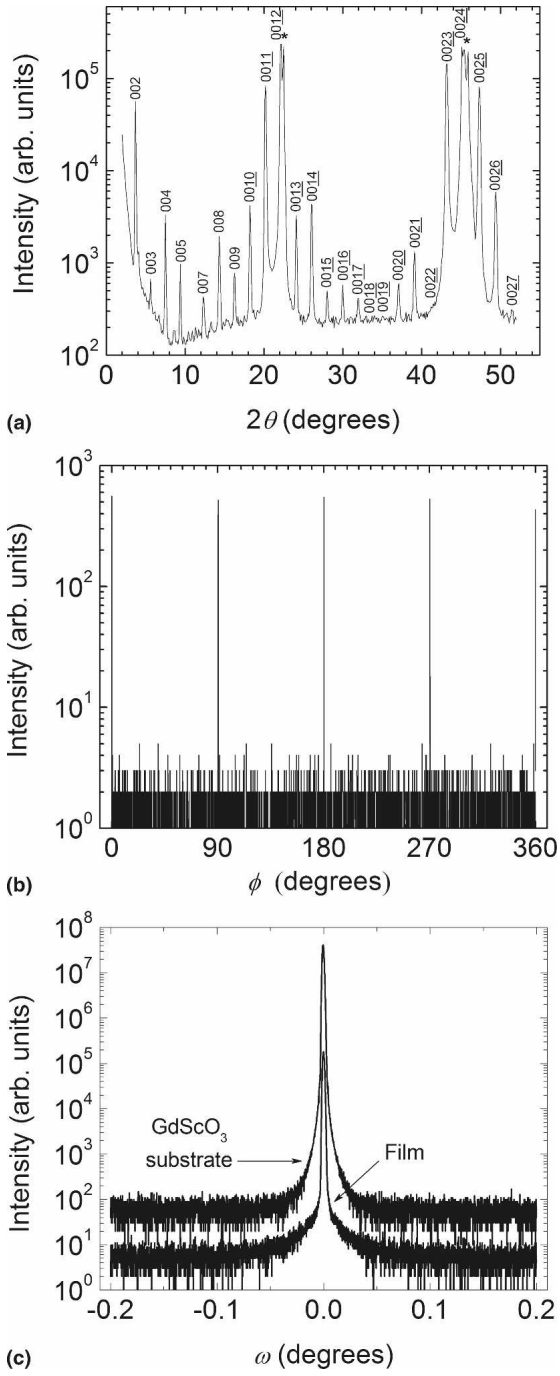

FIG. 18. XRD scans of the $[(BaTiO_3)_8/(SrTiO_3)_4]_{40}$ superlattice grown on (101) $GdScO_3$ substrate (sample no. 25) (a) shows a θ–2θ scan. Substrate peaks are marked with asterisks (*). Nearly all superlattice peaks are present for $2\theta < 55°$, indicating atomically sharp interfaces between $BaTiO_3$ and $SrTiO_3$ layers and accurate periodicity. (b) The in-plane orientation relationship between the $[(BaTiO_3)_8/(SrTiO_3)_4]_{40}$ superlattice and the (101) $GdScO_3$ substrate was determined by a ϕ-scan at $\chi = 42.09°$ of the $10\underline{11}$ superlattice peak. $\phi = 0°$ corresponds to when the in-plane component of the diffraction vector is parallel to the [010] in-plain direction of the $GdScO_3$ substrate. (c) Rocking curves of the $[(BaTiO_3)_8/(SrTiO_3)_4]_{40}$ superlattice. FWHM of 7 arc s (0.0020°) for the superlattice $00\underline{24}$ peak and FWHM of 7 arc s (0.0019°) for the 202 peak of the $GdScO_3$ substrate were measured.

substrates have pseudocubic lattice constants lying between $SrTiO_3$ and $BaTiO_3$. Commensurate $[(BaTiO_3)_n/(SrTiO_3)_m]_p$ superlattices of arbitrary thickness may be grown by the same principles as strained layer superlattices of conventional semiconductors.[34] This enables the growth of much thicker commensurate superlattice structures free of high densities of dislocations. A particular application in need of thick high-quality $[(BaTiO_3)_n/(SrTiO_3)_m]_p$ superlattices is novel phonon devices including mirrors, filters, and cavities that are part of a phonon "laser" architecture.[4] Moreover, the fact that $DyScO_3$, $GdScO_3$, and $SmScO_3$ have large band gaps (>5.5 eV)[35,36] indicates that these substrates are transparent in the UV range allowing forward-scattering UV Raman measurements to be carried out. Such experiments are difficult with $SrTiO_3$ substrates due to its low bandgap (3.2 eV).[37]

The T_C of all superlattices shown in the last column of Table I was obtained from UV Raman measurements.[3]

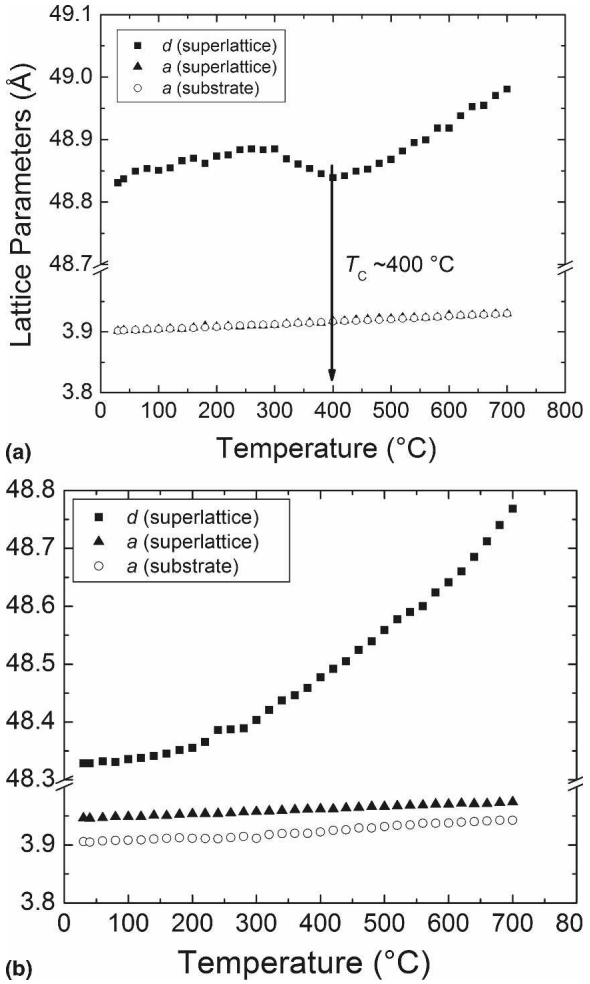

FIG. 19. Temperature dependence of the lattice constants of the (a) commensurate $[(BaTiO_3)_8/(SrTiO_3)_4]_{10}$ superlattice (sample no. 7), (b) partially relaxed $[(BaTiO_3)_8/(SrTiO_3)_4]_{40}$ superlattice (sample no. 14), and $SrTiO_3$ substrate, measured by XRD.

For several samples, the T_C was also determined by temperature-dependent XRD and compared with the UV Raman results. Figure 19 shows the temperature-dependent in-plane and out-of-plane parameters measured by XRD on commensurate sample no. 7 and partially relaxed sample no. 14. Both of these samples have similar $[(BaTiO_3)_8/(SrTiO_3)_4]_p$ structures, but differ in their thicknesses: $p = 10$ and 40, respectively. The in-plane lattice parameters of the underlying $SrTiO_3$ substrates were measured as well and are shown in the plot as open circles. The solid squares and triangles are the measured out-of plane d and in-plane a lattice parameters of the corresponding superlattices. The plot in Fig. 19(a) shows the temperature-dependent XRD of commensurate sample no. 7, a $[(BaTiO_3)_8/(SrTiO_3)_4]_{10}$ superlattice. The $T_C \approx 400$ °C of this sample was determined from the change in slop of the out-of-plane superlattice parameter d as a function of temperature[20–25] and its position is shown by the arrow. For the partially relaxed $[(BaTiO_3)_8/(SrTiO_3)_4]_{40}$ superlattice (sample no. 14) shown in the Fig. 19(b) the in-plane lattice parameters of the superlattice do not overlap with those of the underlying $SrTiO_3$ substrate, indicating that the superlattice has partially relaxed. The T_C of the partially relaxed sample cannot be determined by the temperature-dependent XRD because of the absence of a clear change in the slope of $d(T)$. It is possible, however, to determine the T_C of this partially relaxed sample from UV Raman measurements.[3]

Figure 20 summarizes the T_C of the $[(BaTiO_3)_n/(SrTiO_3)_m]_p$ superlattices measured by UV Raman and in some cases by temperature-dependent XRD. Figure 20(a) shows the dependence of T_C on n and m in $[(BaTiO_3)_n/(SrTiO_3)_m]_p$ superlattices grown on (001) $SrTiO_3$ substrates. The horizontal dashed–dotted line shows the T_C of bulk (unstrained) $BaTiO_3$. The data in Fig. 20(a) show that in nanoscale commensurate $[(BaTiO_3)_n/(SrTiO_3)_m]_p$ superlattices grown on (001) $SrTiO_3$ substrates the T_C strongly depend on the superlattice structure and thickness n of individual $BaTiO_3$ layers. The large variation of T_C from ~170 K (sample no. 15) to ~640 K (sample no. 7) is a result of competing finite size effects in these superlattices. It can be seen that T_C increases with n and decreases with m.[3] The curves in Fig. 20(a) are from three-dimensional phase-field calculations that allow the $[(BaTiO_3)_n/(SrTiO_3)_m]_p$ superlattice to break up into small domains (their lowest-energy configuration). These calculations that use the physical properties of $BaTiO_3$ and $SrTiO_3$ single crystals [i.e., are not fit to the experimental data in Fig. 20(a)] are described in detail elsewhere.[3,38,39]

Figure 20(b) shows the dependence of T_C on the mismatch strain ϵ in the $BaTiO_3$ layers for superlattices with the same $[(BaTiO_3)_8/(SrTiO_3)_4]_p$ structure grown on (001) $SrTiO_3$, (101) $DyScO_3$, (101) $GdScO_3$, and (101) $SmScO_3$ substrates. This plot emphasizes the influence of mismatch strain on T_C. The highest T_C is observed in the $[(BaTiO_3)_8/(SrTiO_3)_4]_p$ superlattice subjected to the largest compressive strain (~2.3%). As the strain decreases, the T_C decreases toward its value in unstrained bulk $BaTiO_3$. The horizontal dashed–dotted line in this plot shows the T_C of bulk $BaTiO_3$ for comparison. Thus,

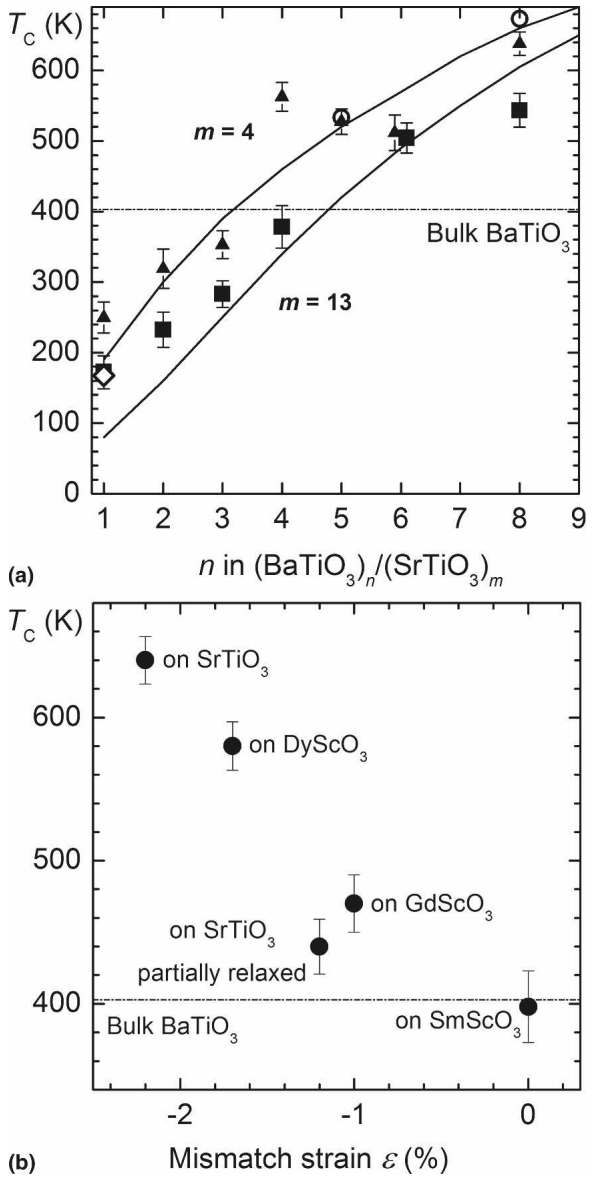

FIG. 20. Summary plot of the T_C obtained from UV Raman measurements. (a) Shows the dependence of T_C on n and m in $[(BaTiO_3)_n/(SrTiO_3)_m]_p$ superlattices grown on (001) $SrTiO_3$ substrates. Solid triangles are for $m = 4$, solid squares are for $m = 13$, and the open diamond symbol is for $m = 30$. Open circles are from temperature-dependent XRD measurements. Lines are from three-dimensional phase-field model calculations for $m = 4$ and $m = 13$ and the horizontal dashed–dotted line shows the T_C of bulk (unstrained) $BaTiO_3$. (b) Dependence of T_C on the mismatch strain ϵ on the $BaTiO_3$ layers in the superlattices with the same $[(BaTiO_3)_8/(SrTiO_3)_4]_p$ structure grown on (001) $SrTiO_3$, (101) $DyScO_3$, (101) $GdScO_3$, and (101) $SmScO_3$ substrates (sample nos. 7, 24, 25, 26).

$DyScO_3$, $GdScO_3$, and $SmScO_3$ substrates not only significantly improve the crystallinity of the $[(BaTiO_3)_n/(SrTiO_3)_m]_p$ superlattices, but also can be used to tune the T_C via strain. Detailed UV Raman measurements on these $[(BaTiO_3)_n/(SrTiO_3)_m]_p$ superlattices in combination with first-principles calculations have shown that the unstrained $SrTiO_3$ layers in commensurate $BaTiO_3/SrTiO_3$ superlattices grown on $SrTiO_3$ substrates are poled by the neighboring ferroelectric $BaTiO_3$ layers, while the strained $SrTiO_3$ layers in $BaTiO_3/SrTiO_3$ superlattices grown on $DyScO_3$, $GdScO_3$, and $SmScO_3$ substrates are not only polar, but also exhibit strain-induced ferroelectricity.[3,40]

IV. CONCLUSIONS

We have used shuttered RHEED intensity oscillations to precisely grow a series of $[(BaTiO_3)_n/(SrTiO_3)_m]_p$ superlattices by reactive MBE on (001) $SrTiO_3$, (101) $DyScO_3$, (101) $GdScO_3$, and (101) $SmScO_3$ substrates. Structural characterization by XRD and HRTEM demonstrate the synthesis of commensurate nanoscale superlattices with excellent crystalline quality and atomically abrupt interfaces. The mosaic spread of superlattices depends not only on the growth parameters and mismatch strain, but also on the structural perfection of the underlying substrate. By using new $DyScO_3$, $GdScO_3$, and $SmScO_3$ substrates we have shown that the structural perfection of $[(BaTiO_3)_n/(SrTiO_3)_m]_p$ superlattices can be drastically improved. Ferroelectricity was observed in $BaTiO_3/SrTiO_3$ superlattices containing as few as one $BaTiO_3$ layer in the repeated superlattice structural unit, i.e., a $BaTiO_3$ layer just 4 Å thick. The combination of finite size and strain effects was seen to shift the T_C of commensurate $[(BaTiO_3)_n/(SrTiO_3)_m]_p$ superlattices over a 500 K range.

ACKNOWLEGMENTS

We gratefully acknowledge D.H.A. Blank for informing us of his termination method for (101) $DyScO_3$ substrates. This work was supported by the Office of Naval Research under Grants N00014-03-1-0721 (D.G. Schlom), N00014-04-1-0426 (D.G. Schlom), and N00014-05-1-0559 (C.B. Eom) monitored by Dr. Colin Wood; by the National Science Foundation (NSF) under Grants DMR-0507146 (D.G. Schlom, L.Q. Chen, X.Q. Pan, C.B. Eom, and X.X. Xi), DMR-0705127 (D.A. Tenne), DMR-0122638 (L.Q. Chen), DMR-0213623 (L.Q. Chen), DMR-0313764 (C.B. Eom), ECS-0210449 (C.B. Eom), and DMR-0315633 (X.Q. Pan); by the United States Department of Energy (DOE) under Grant DE-FG02-01ER45907 (X.X. Xi); Research corporation under Grant No. 7134 (D.A. Tenne); by a Guggenheim fellowship (L.Q. Chen); and by NASA under Grant NASA3-NCC1034 (R.S.K).

REFERENCES

1. J.B. Neaton and K.M. Rabe: Theory of polarization enhancement in epitaxial $BaTiO_3/SrTiO_3$ superlattices. *Appl. Phys. Lett.* **82,** 1586 (2003).
2. K. Johnston, X. Huang, J.B. Neaton, and K.M. Rabe: First-principles study of symmetry lowering and polarization in $BaTiO_3/SrTiO_3$ superlattices with in-plane expansion. *Phys. Rev. B* **71,** 100103 (2005).
3. D.A. Tenne, A. Bruchhausen, N.D. Lanzillotti-Kimura, A. Fainstein, R.S. Katiyar, A. Cantarero, A. Soukiassian, V. Vaithyanathan, J.H. Haeni, W. Tian, D.G. Schlom, K.J. Choi, D.M. Kim, C.B. Eom, H.P. Sun, X.Q. Pan, Y.L. Li, L.Q. Chen, Q.X. Jia, S.M. Nakhmanson, K.M. Rabe, and X.X. Xi: Probing nanoscale ferroelectricity by ultraviolet Raman spectroscopy. *Science* **313,** 1614 (2006).
4. A. Soukiassian, W. Tian, D.A. Tenne, X.X. Xi, D.G. Schlom, N.D. Lanzillotti-Kimura, A. Bruchhausen, A. Fainstein, H.P. Sun, X.P. Pan, A. Cros, and A. Cantarero: Acoustic Bragg mirrors and cavities made using piezoelectric oxides. *Appl. Phys. Lett.* **90,** 042909 (2007).
5. H.P. Sun, W. Tian, X.Q. Pan, J.H. Haeni, and D.G. Schlom: Evolution of dislocation arrays in epitaxial $BaTiO_3$ thin films grown on (100) $SrTiO_3$. *Appl. Phys. Lett.* **84,** 3298 (2004).
6. D. Taylor: Thermal-expansion data VIII complex oxides, ABO_3, the perovskites. *Trans. J. Br. Ceram. Soc.* **84,** 181 (1985).
7. R. Ueckera, H. Wilke, D.G. Schlom, B. Velickov, P. Reiche, A. Polity, M. Bernhagen, and M. Rossberg: Spiral formation during Czochralski growth of rare-earth scandates. *J. Cryst. Growth* **295,** 84 (2006).
8. B. Velickov, V. Kahlenberg, R. Bertram, and M. Bernhagen: Crystal chemistry of $GdScO_3$, $DyScO_3$, $SmScO_3$, and $NdScO_3$. *Z. Kristallogr.* **222,** 466 (2007).
9. C.D. Theis and D.G. Schlom: Cheap and stable titanium source for use in oxide molecular beam epitaxy systems. *J. Vac. Sci. Technol., A* **14,** 2677 (1996).
10. K. Iijima, T. Terashima, Y. Bando, K. Kamigaki, and H. Terauchi: Atomic layer growth of oxide thin films with perovskite-type structure by reactive evaporation. *J. Appl. Phys.* **72,** 2840 (1992).
11. T. Tsurumi, T. Suzuki, M. Yamane, and M. Daimon: Fabrication of barium titanate/strontium titanate artificial superlattice by atomic layer epitaxy. *Jpn. J. Appl. Phys.*, Pt. 1 **33,** 5192 (1994).
12. J.H. Haeni: Nanoengineering of Ruddlesden-Popper phases using molecular beam epitaxy. Ph.D. Thesis, The Pennsylvania State University, 2002, pp. 60–86.
13. G. Koster, B.L. Kropman, G.J.H.M. Rijnders, and D.H.A. Blank: Quasi-ideal strontium titanate crystal surfaces through formation of strontium hydroxide. *Appl. Phys. Lett.* **73,** 2920 (1998).
14. T. Kubo and H. Nozoye: Surface structure of $SrTiO_3$ (100). *Surf. Sci.* **542,** 177 (2003).
15. M.R. Castell: Scanning tunneling microscopy of reconstructions on the $SrTiO_3$ (001) surface. *Surf. Sci.* **505,** 1 (2002).
16. J.H. Haeni, C.D. Theis, and D.G. Schlom: RHEED intensity oscillations for the stoichiometric growth of $SrTiO_3$ thin films by reactive molecular beam epitaxy. *J. Electroceram.* **4,** 385 (2000).
17. *Landolt-Börnstein: Numerical Data and Functional Relationships in Science and Technology*, edited by K-H. Hellwege and A.M. Hellwege, New Series, Group III, Vol. 16a (Springer, New York, 1981), p. 59.
18. P. Bodin, S. Sakai, and Y. Kasai: Molecular-beam epitaxy fabrication of $SrTiO_3$ and $Bi_2Sr_2CaCu_2O_8$ heterostructures using a novel reflection high-energy electron-diffraction monitoring technique. *Jpn. J. Appl. Phys.*, Pt. 2 **31**, 949 (1992).
19. D.H.A. Blank: (private communication).
20. K.J. Choi, M. Biegalski, Y.L. Li, A. Sharan, J. Schubert, R. Uecker, P. Reiche, Y.B. Chen, X.Q. Pan, V. Gopalan,

L-Q. Chen, D.G. Schlom, and C.B. Eom: Enhancement of ferroelectricity in strained $BaTiO_3$ thin films. *Science* **306,** 1005 (2004).
21. E.D. Specht, H-M. Christen, D.P. Norton, and L.A. Boatner: X-ray diffraction measurement of the effect of layer thickness on the ferroelectric transition in epitaxial $KTaO_3/KNbO_3$ multilayers. *Phys. Rev. Lett.* **80,** 4317 (1998).
22. H-M. Christen, E.D. Specht, D.P. Norton, M.F. Chisholm, and L.A. Boatner: Long-range ferroelectric interactions in $KTaO_3/KNbO_3$ superlattice structures. *Appl. Phys. Lett.* **72,** 2535 (1998).
23. S.K. Streiffer, J.A. Eastman, D.D. Fong, C. Thompson, A. Munkholm, M.V.R. Murty, O. Auciello, G.R. Bai, and G.B. Stephenson: Observation of nanoscale 180° stripe domains in ferroelectric $PbTiO_3$ thin films. *Phys. Rev. Lett.* **89,** 067601 (2002).
24. M. Sepliarsky, S.R. Phillpot, M.G. Stachiotti, and R.L. Migoni: Ferroelectric phase transitions and dynamical behavior in $KNbO_3/KTaO_3$ superlattices by molecular-dynamics simulation. *J. Appl. Phys.* **91,** 3165 (2002).
25. D.G. Schlom, L.Q. Chen, C.B. Eom, K.M. Rabe, S.K. Streiffer, and J.M. Triscone: Strain tuning of ferroelectric thin films. *Annu. Rev. Mater. Res.* **37,** 589 (2007).
26. J.B. Nelson and D.P. Riley: An experimental investigation of extrapolation methods in the derivation of accurate unit-cell dimensions of crystals. *Proc. Phys. Soc. London* **57,** 160 (1945).
27. C. Brooks, W. Tian, and D.G. Schlom: (unpublished).
28. J.H. Haeni, P. Irvin, W. Chang, R. Uecker, P. Reiche, Y.L. Li, S. Choudhury, W. Tian, M.E. Hawley, B. Craigo, A.K. Tagantsev, X.Q. Pan, S.K. Streiffer, L.Q. Chen, S.W. Kirchoefer, J. Levy, and D.G. Schlom: Room-temperature ferroelectricity in strained $SrTiO_3$. *Nature* **430,** 758 (2004).
29. M.D. Biegalski, Y. Jia, D.G. Schlom, S. Trolier-McKinstry, S.K. Streiffer, V. Sherman, R. Uecker, and P. Reiche: Relaxor ferroelectricity in strained epitaxial $SrTiO_3$ thin films on $DyScO_3$ substrates. *Appl. Phys. Lett.* **88,** 192907 (2006).
30. A. Vasudevarao, A. Kumar, L. Tian, J.H. Haeni, Y.L. Li, C-J. Eklund, Q.X. Jia, R. Uecker, P. Reiche, K.M. Rabe, L.Q. Chen, D.G. Schlom, and V. Gopalan: Multiferroic domain dynamics in strained strontium titanate. *Phys. Rev. Lett.* **97,** 257602 (2006).
31. H.J. Scheel, J.G. Bednorz, and P. Dill: Crystal growth of strontium titanate $SrTiO_3$. *Ferroelectrics* **13,** 507 (1976).
32. S.B. Qadri, J.S. Horwitz, D.B. Chrisey, R.C.Y. Auyeung, and K.S. Grabowski: X-ray characterization of extremely high-quality $(Sr,Ba)TiO_3$ films grown by pulsed laser deposition. *Appl. Phys. Lett.* **66,** 1605 (1995).
33. P.I. Nabokin, D. Souptel, and A.M. Balbashov: Floating zone growth of high-quality $SrTiO_3$ single crystals. *J. Cryst. Growth* **250,** 397 (2003).
34. J.W. Mathews: *Epitaxial Growth*, edited by J.W. Mathews, Vol. 2 (Academic Press, New York 1975).
35. D.G. Schlom and J.H. Haeni: A thermodynamic approach to selecting alternative gate dielectrics. *MRS Bull.* **27,** 198 (2002).
36. S.G. Lim, S. Kriventsov, T.N. Jackson, J.H. Haeni, D.G. Schlom, A.M. Balbashov, R. Uecker, P. Reiche, J.L. Freeouf, and G. Lucovsky: Dielectric functions and optical bandgaps of high-K dielectrics for metal-oxide-semiconductor field-effect transistors by far ultraviolet spectroscopic ellipsometry. *J. Appl. Phys.* **91,** 4500 (2002).
37. M. Cardona: Optical properties and band structure of $SrTiO_3$ and $BaTiO_3$. *Phys. Rev.* **140,** 651 (1965).
38. Y.L. Li, S.Y. Hu, D. Tenne, A. Soukiassian, X.X. Xi, D.G. Schlom, K.J. Choi, C.B. Eom, A. Saxena, T. Lookman, Q.X. Jia, and L.Q. Chen: Prediction of ferroelectricity in $BaTiO_3/SrTiO_3$ superlattices with domains. *Appl. Phys. Lett.* **91,** 112914 (2007).
39. Y.L. Li, S.Y. Hu, D. Tenne, A. Soukiassian, D.G. Schlom, L.Q. Chen, X.X. Xi, K.J. Choi, C.B. Eom, A. Saxena, T. Lookman, and Q.X. Jia: Interfacial coherency and ferroelectricity of $BaTiO_3/SrTiO_3$ superlattice films. *Appl. Phys. Lett.* **91,** 252904 (2007).
40. D. Tenne, J.D. Schmidt, P. Turner, A. Soukiassian, X.X. Xi, D.G. Schlom, Y.L. Li, Q.X. Jia, L.Q. Chen, M. Bernhagen, P. Reiche, and R. Uecker: (unpublished).